Nano Research

Open Access

Research Article

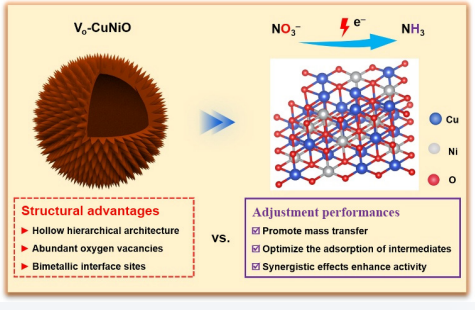
Synergistic effect of oxygen vacancies and oxygen-bridged multi-interface sites for high-performance electrocatalytic nitrate reduction to ammonia

Li Qin[1,2], Zixuan Tong[2], Guiqin Chen[2], Qiqi Zhou[2], Chengxiang Liu[2], Yuxi Wu[1], Mingfu Ye[2,3,4], Binbin Jiang[4], Yiwei Tan[3], Guozheng Huang[1]✉, Guohong Fan[2]✉, and Konglin Wu[2,4,5]✉

[1] *Key Laboratory of Metallurgical Emission Reduction & Resources Recycling of Ministry of Education, Anhui University of Technology, Maanshan 243032, China*
[2] *Institute of Clean Energy and Advanced Nanocatalysis (iClean), School of Chemistry and Chemical Engineering, Anhui University of Technology, Maanshan 243032, China*
[3] *State Key Laboratory of Materials-Oriented Chemical Engineering, Nanjing University of Technology, Nanjing 211816, China*
[4] *Anhui Provincial Key Laboratory of Advanced Catalysis and Energy Materials, School of Chemistry and Chemical Engineering, Anqing Normal University, Anqing 246011, China*
[5] *State Key Laboratory of Heavy Oil Processing, China University of Petroleum (East China), Qingdao 266580, China*

Cite this article: *Nano Research*, **2026**, *19*, 94908769. https://doi.org/10.26599/NR.2026.94908769

ABSTRACT: In recent years, the development of highly efficient electrocatalysts for the nitrate reduction reaction (NO_3RR) to ammonia (NH_3) has become essential for achieving sustainable nitrogen cycling. Herein, a sea urchin-like CuNiO with oxygen vacancies (V_o-CuNiO) was synthesized via a gas-assisted solvothermal method followed by calcination. This unique hierarchical architecture facilitates the formation of abundant oxygen vacancies and optimizes the adsorption of key intermediates, while the exposure of oxygen-bridged multi-interface sites (such as Cu–O–Cu, Ni–O–Ni, and Cu–O–Ni interfacial sites) enhances mass transport. The obtained V_o-CuNiO-350 catalyst exhibited exceptional performance in the electrocatalytic NO_3RR to NH_3 under neutral conditions, achieving a peak NH_3 Faradaic efficiency (FE) of 94.9% at −0.8 V vs. reversible hydrogen electrode (RHE) and a maximum NH_3 yield rate of 480.9 μmol·h^{-1}·cm^{-2} at −1.0 V vs. RHE. *In-situ* attenuated total reflection Fourier transform infrared (ATR-FTIR) spectroscopy and density functional theory (DFT) calculations indicated that the oxygen vacancies and bimetallic interface sites in the V_o-CuNiO-350 catalyst provide a synergistic effect to enhance NO_3RR performance. Specifically, the oxygen vacancies and the newly constructed Cu–O–Ni interface sites optimize the adsorption of intermediates and promote the reduction of NO_3^- to NH_3. The further continuous electrocatalytic NH_3 synthesis tests indicate that this catalyst can achieve high-purity NH_4Cl production at a rate of 14.0 mg·h^{-1}. Moreover, in a self-assembled Zn-NO_3^- hybrid battery, an output power density of 2.88 mW·cm^{-2} was attained, thereby enabling simultaneous electricity generation and NH_3 synthesis. This work demonstrates a viable pathway for converting nitrate from wastewater into ammonia while co-producing electrical energy.



KEYWORDS: hollow nanostructures, bimetallic interface sites, electrocatalysis, ammonia synthesis

1 Introduction

Ammonia (NH_3) is fundamental to modern industry and agriculture. It serves as the primary precursor for nitrogen-based fertilizers and supports global food security [1–3]. In the context of carbon neutrality, ammonia is also regarded as a highly promising carbon free energy carrier and hydrogen vector owing to its high energy density (4.3 kWh·kg^{-1}) [4], ease of liquefaction and storage, and zero-carbon emissions during combustion [5–7]. However, the currently dominant Haber–Bosch process has major drawbacks. It relies heavily on fossil fuels, requires high energy input (consuming 1%–2% of global energy), and produces significant CO_2 emissions. These limitations conflict with the global pursuit of carbon

Received: March 23, 2026; **Revised:** April 22, 2026
Accepted: April 22, 2026

✉Address correspondence to Guozheng Huang, guozheng.huang@ahut.edu.cn; Guohong Fan, ghfan8@ahut.edu.cn; Konglin Wu, klwuchem@ahut.edu.cn

neutrality [8–10]. Consequently, developing novel and green ammonia synthesis technologies powered by renewable electricity under mild conditions is of great strategic importance. In this context, the electrocatalytic nitrate reduction reaction (NO_3RR) has recently emerged as a promising alternative. This approach uses NO_3^- pollutants from wastewater as the nitrogen source and enables their efficient and selective conversion into value-added ammonia, thereby achieving simultaneous pollution remediation and resource recovery [11–16]. This strategy not only offers a new pathway for sustainable ammonia production but also provides an effective solution for nitrate pollution control.

Among various candidate materials, Cu-based catalysts have attracted significant attention as efficient monometallic systems for the electrocatalytic NO_3RR to NH_3. This is mainly due to their strong ability to adsorb and activate NO_3^-, as well as their excellent electrical conductivity [17–21]. However, monometallic Cu catalysts are often limited by low product selectivity and insufficient operational stability [22]. These drawbacks arise from the complex and multi-step reaction pathway, in which improper adsorption of key intermediates can favor the formation of undesired byproducts. Furthermore, Cu active sites are prone to deactivation or surface reconstruction under the high over potentials typically required for NO_3RR [23–28]. To address these issues, the design of Cu-based bimetallic catalysts has been widely explored. Incorporating a second metal can modulate the electronic structure and optimize the electron density at the Cu sites. This adjustment enables precise tuning of the adsorption energies of NO_3^- and key reaction intermediates, thereby directing the reaction pathway toward ammonia formation [29–34]. At the same time, the second metal introduces synergistic active sites that help suppress competing side reactions and improve overall catalytic performance. Bimetallic interactions can also inhibit the aggregation of Cu species and improve the overall structural stability of the catalyst under operating conditions [9, 33, 35, 36]. As a result, recent studies have shown that, through precise control of bimetallic composition, interfacial structure, and electronic states, Cu-based bimetallic catalysts can deliver outstanding performance, thereby achieving NH_3 Faradaic efficiencies (FEs) above 95% together with high production rates [37–43]. Despite these encouraging advances, several critical issues remain unresolved, including the precise regulation of specific bimetallic systems, the exact nature of the interfacial active sites, and a deeper mechanistic understanding of the reaction pathways. These challenges warrant further systematic investigation.

In this work, a sea urchin-like CuNiO with oxygen vacancies (V_o-CuNiO) and oxygen-bridged multi-interface sites (such as Cu–O–Cu, Ni–O–Ni, and Cu–O–Ni interfacial sites) was synthesized through a gas-assisted solvothermal method followed by calcination. The samples obtained at different calcination temperatures are denoted as V_o-CuNiO-*T*, where *T* represents the calcination temperature (250, 300, 350, 400, and 450 °C). The electrocatalytic performance of the obtained catalysts toward the NO_3RR for NH_3 production was systematically evaluated under neutral conditions (0.5 M Na_2SO_4 + 0.1 M $NaNO_3$). On the one hand, *in-situ* attenuated total reflection Fourier-transform infrared (ATR-FTIR) spectroscopy was employed to monitor the intermediate species formed during the NO_3RR process. On the other hand, density functional theory (DFT) calculations were conducted to clarify the crucial roles of oxygen vacancies and interfacial sites and to reveal the origin of the catalyst's intrinsic activity. The continuous electrocatalytic NH_3 synthesis capacity of the V_o-CuNiO-350 catalyst was further evaluated in the form of NH_4Cl. Additionally, the electrochemical performance of a self-assembled Zn-NO_3^- hybrid battery using V_o-CuNiO-350 as the cathode and Zn foil as the anode was systematically investigated.

2 Results and discussion

As illustrated in Fig. 1(a), V_o-CuNiO and bimetallic interface sites were synthesized via a gas-assisted solvothermal method followed by calcination in air (detailed experimental procedures are provided in the Electronic Supplementary Material (ESM)). First, the Cu-Ni precursors were prepared using a gas-assisted soft-template solvothermal approach [44]. The morphology of the resulting Cu-Ni precursors was characterized by scanning electron microscopy (SEM) and transmission electron microscopy (TEM). The SEM (Figs. 1(b) and 1(c)) and TEM (Fig. 1(d)) images reveal that the Cu-Ni precursors exhibit a well-defined sea urchin-like structure. The particle size of the sea urchin-like Cu-Ni precursors ranges from 700 to 1000 nm (Fig. S1 in the ESM). The crystal structure of the as-prepared materials was examined by X-ray diffraction (XRD). As shown in Fig. S2 in the ESM, the diffraction peaks of the Cu-Ni precursors correspond to $(Cu, Ni)_2CO_3(OH)_2$ (JCPDS No. 27-0178) [45], $Cu_2(NO_3)(OH)_3$ (JCPDS No. 45-0594), and $Ni_3(NO_3)_2(OH)_4$ (JCPDS No. 22-0752) [46]. The sea urchin-like Cu-Ni precursors were then calcined at 350 °C to produce V_o-CuNiO-350. After calcination in air, V_o-CuNiO-350 retains its urchin-like spherical morphology without noticeable structural collapse (Figs. 1(e)–1(g)). XRD analysis indicates that the resulting V_o-CuNiO-350 is a Cu-rich oxide phase, which includes CuO (JCPDS No. 45-0937), NiO (JCPDS No. 47-1047), and $NiCuO_2$ (JCPDS No. 06-0720) (Fig. S3 in the ESM). These XRD results indicate that it is possible to construct new Cu–O–Ni interface unit due to the pyrolysis of $(Cu, Ni)_2CO_3(OH)_2$ components in the sea urchin-like Cu-Ni precursors [47, 48]. The high-resolution TEM (HRTEM) image shows that V_o-CuNiO-350 has very high crystallinity, with a lattice spacing of 0.24 nm corresponding to the (111) plane of CuO (Fig. 1(h)). The selected area electron diffraction (SAED) pattern reveals that V_o-CuNiO-350 has a polycrystalline structure, confirming that its sea urchin-like morphology is made up of small nanocrystals (Fig. S4 in the ESM). The high-angle annular dark-field scanning transmission electron microscopy (HAADF-STEM) image (Fig. 1(i)) shows that the product has a hollow structure, consistent with the TEM results (Fig. 1(g)). Additionally, the elemental surface distribution was analyzed using energy-dispersive X-ray (EDX) spectroscopy. As shown in Fig. 1(j), Cu, Ni, and O are uniformly distributed on the surface of the sea urchin-like hollow structure, further confirming that V_o-CuNiO-350 is a uniform Ni-doped CuO structure. Inductively coupled plasma optical emission spectrometry (ICP-OES) results show that the mass percentages of Cu and Ni in V_o-CuNiO-350 are 64.18% and 21.65%, respectively, corresponding to an atomic ratio of 2.74:1 (Table S1 in the ESM). Additionally, V_o-CuNiO-T samples were prepared at different calcination temperatures, including V_o-CuNiO-250 (Figs. S5(a) and S5(b) in the ESM), V_o-CuNiO-300 (Figs. S5(c) and S5(d) in the ESM), V_o-CuNiO-400 (Figs. S5(e) and S5(f) in the ESM), and V_o-CuNiO-450 (Figs. S5(g) and S5(h)). For comparison, using the same synthesis method, pure copper oxide and nickel oxide with oxygen vacancies were also synthesized, and they were named as V_o-CuO-350 (Fig. S6 in the ESM) and V_o-NiO-350 (Fig. S7 in the ESM), respectively.

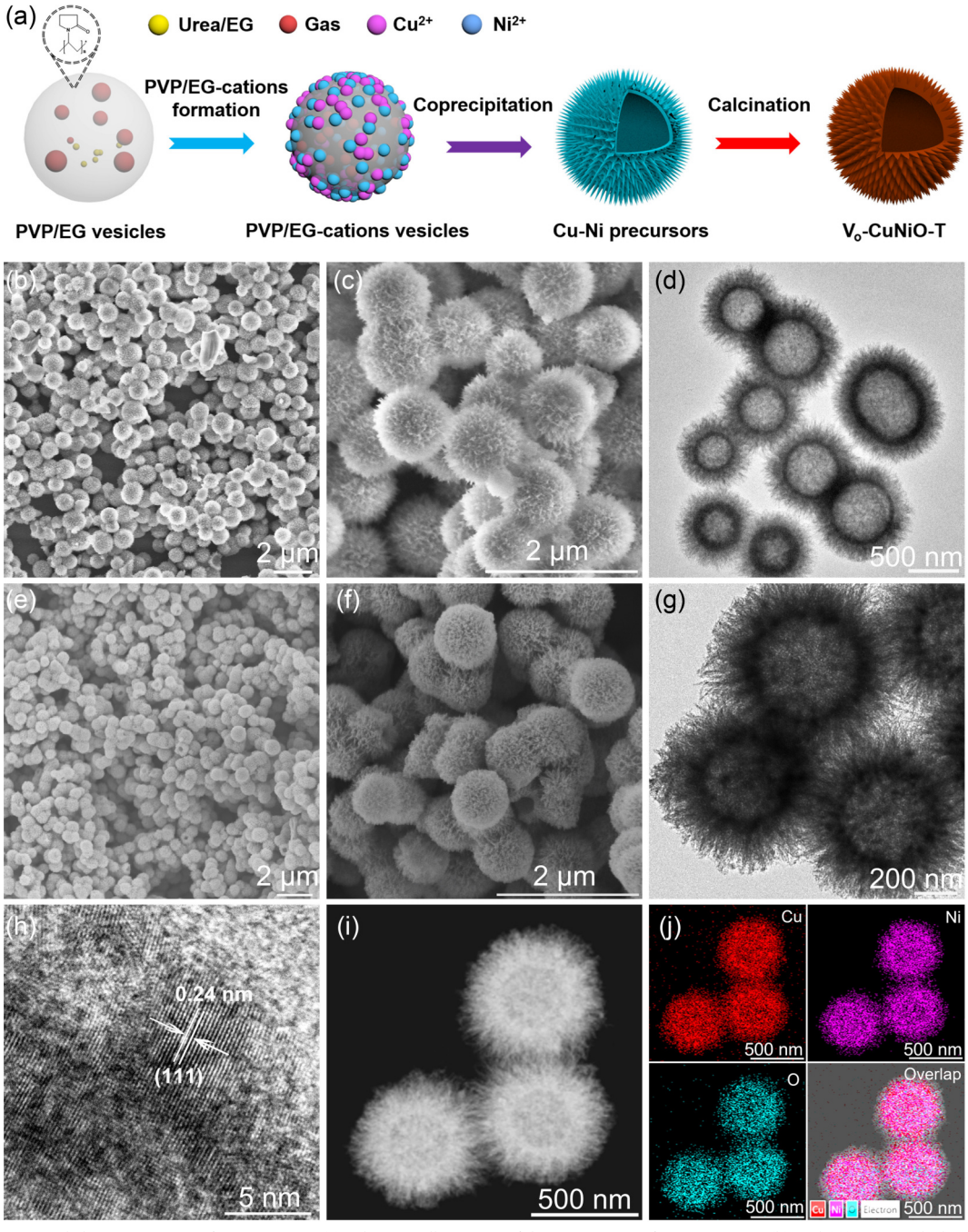


Figure 1 Preparation and characterizations of V_o-CuNiO-T. (a) Schematic illustration of the preparation of V_o-CuNiO-T. ((b) and (c)) SEM and (d) TEM images of sea urchin-like Cu-Ni precursors. ((e) and (f)) SEM and (g) TEM images of V_o-CuNiO-350. (h) HRTEM image of V_o-CuNiO-350. (i) HAADF-STEM and corresponding (j) EDX elemental mapping images of V_o-CuNiO-350.

Furthermore, the pore structure of the samples was investigated using N_2 adsorption–desorption measurements. The specific surface area, pore volume, and pore size of the catalysts were determined using the Brunauer–Emmett–Teller (BET) and Barrett–Joyner–Halenda (BJH) methods, respectively. As shown in Fig. S8 and Table S2 in the ESM, V_o-CuNiO-350 has a larger BET specific surface area (110.6 $m^2 \cdot g^{-1}$) and a higher pore volume (0.33 $cm^3 \cdot g^{-1}$) compared with the pure V_o-CuO-350 and V_o-NiO-350. The pore size distribution suggests that the pores mainly originate from pyrolysis and particle accumulation. X-ray photoelectron spectroscopy (XPS) was used to examine the surface electronic structure and chemical states of elements in the V_o-CuNiO-350, V_o-CuO-350, and V_o-NiO-350. According to the high-resolution spectra of Cu, Ni, and O, the chemical states of these elements were determined from the fitting results (Table S3 in the ESM). The survey spectrum confirms the presence of Cu, Ni, and O on the surface (Fig. S9 in the ESM). The high-resolution Cu 2p spectra of V_o-CuNiO-350 and V_o-CuO-350 are shown in Fig. 2(a), revealing two distinct satellite peaks. For V_o-CuNiO-350, the binding energies of Cu $2p_{3/2}$ and Cu $2p_{1/2}$ are 932.8 and 934.7 eV, and 952.5 and 954.5 eV, respectively, while for V_o-CuO-350, they are 933.5 and 934.8 eV, and 952.8 and 954.6 eV, respectively

[49, 50]. The shift of Cu binding energies to lower values upon Ni introduction indicates charge transfer between Cu and Ni in V_o-CuNiO-350. The Ni 2p spectra exhibit characteristic doublets for Ni $2p_{3/2}$ and Ni $2p_{1/2}$ along with satellite peaks for V_o-CuNiO-350 and V_o-NiO-350 (Fig. 2(b)). In V_o-CuNiO-350, the fitted peaks at 854.1 and 871.8 eV are assigned to Ni^{2+}, while those at 856.1 and 874.0 eV correspond to Ni^{3+} [51, 52]. Compared with Ni in pure V_o-NiO-350, the formation of Cu-Ni oxide leads to a shift of Ni binding energy to higher values, owing to electron redistribution caused by the introduction of highly electronegative Cu. The high-resolution O 1s spectra of V_o-CuNiO-350, V_o-CuO-350, and V_o-NiO-350 can be deconvoluted into three components, corresponding to lattice oxygen, V_o, and surface-adsorbed oxygen species, respectively (Fig. 2(c)) [53]. Compared with pure V_o-CuO-350 and V_o-NiO-350, V_o-CuNiO-350 shows a decreased proportion of lattice oxygen (Fig. 2(c)), indicating that the Cu-Ni bimetallic composite reduces lattice oxygen content and generates more active oxygen sites [54]. These XPS results demonstrate that Ni introduction induces electron transfer between Cu and Ni in the sea urchin-like V_o-CuNiO-350, thereby providing a foundation for the formation of highly active Cu–O–Ni interface sites [55]. The oxygen vacancy concentrations of the samples were further examined using electronic paramagnetic resonance (EPR). As shown in Fig. 2(d), the strong EPR signals at g = 2.003 are attributed to surface electrons trapped in oxygen vacancies [56, 57]. The signal intensity of V_o-CuNiO-350 is significantly higher than that of V_o-CuO-350 and V_o-NiO-350, indicating a higher concentration of oxygen vacancies, consistent with the XPS results (Fig. 2(c)).

To investigate the local chemical environment of V_o-CuNiO-350, extended X-ray absorption fine structure (EXAFS) and X-ray absorption near-edge structure (XANES) analyses were conducted. The Cu K-edge XANES spectrum of V_o-CuNiO-350 lies between those of Cu foil and CuO, indicating a Cu oxidation state between 0 and +2 (Fig. 3(a)) and closer to +2. In the *R*-space Fourier-transform EXAFS spectrum (Fig. 3(b)), the main peak at ~ 1.5 Å corresponds to the Cu–O coordination shell, while a smaller feature between 2.2 and 2.5 Å suggests weak Cu–O–Cu interactions. EXAFS fitting results show that each Cu center is coordinated by four O atoms, forming CuO_4 units (Fig. 3(c) and Table S4 in the ESM). Similarly, the Ni K-edge XANES (Fig. 3(d)) and EXAFS (Fig. 3(e)) spectra indicate that Ni species are positively charged, with O atoms dominating their first coordination shell, as confirmed by EXAFS fitting analyses (Fig. 3(f) and Table S5 in the ESM). Wavelet transform (WT) analysis further confirms that Cu experiences contributions from both Cu–O and Cu–O–Cu interactions (Figs. 3(g)–3(i)), while Ni shows contributions from Ni–O and Ni–O–Ni interactions (Figs. 3(j)–3(l)). According to these comprehensive characterizations, the proposed structures of V_o-CuNiO-350 (Fig. 3(m)), V_o-CuO-350 (Fig. 3(n)), and V_o-NiO-350 (Fig. 3(o)) are presented. Therefore, urchin-like V_o-CuNiO-350 hollow hierarchical nanostructures with abundant oxygen vacancies and three different oxygen-bridged multi-interface sites (such as Cu–O–Cu, Ni–O–Ni, and Cu–O–Ni interfacial sites) were successfully synthesized.

To evaluate the performance of the synthesized catalysts, electrocatalytic NO_3RR to NH_3 was used as a model reaction. The tests were conducted in an H-type electrolytic cell with a three-electrode system, using 0.5 M Na_2SO_4 containing 0.1 M $NaNO_3$ as the electrolyte. The concentrations of NH_3 and the intermediate NO_2^- were determined by ultraviolet–visible (UV–vis) spectrophotometry (Fig. S10 in the ESM). First, linear sweep voltammetry (LSV) was used to preliminarily assess the

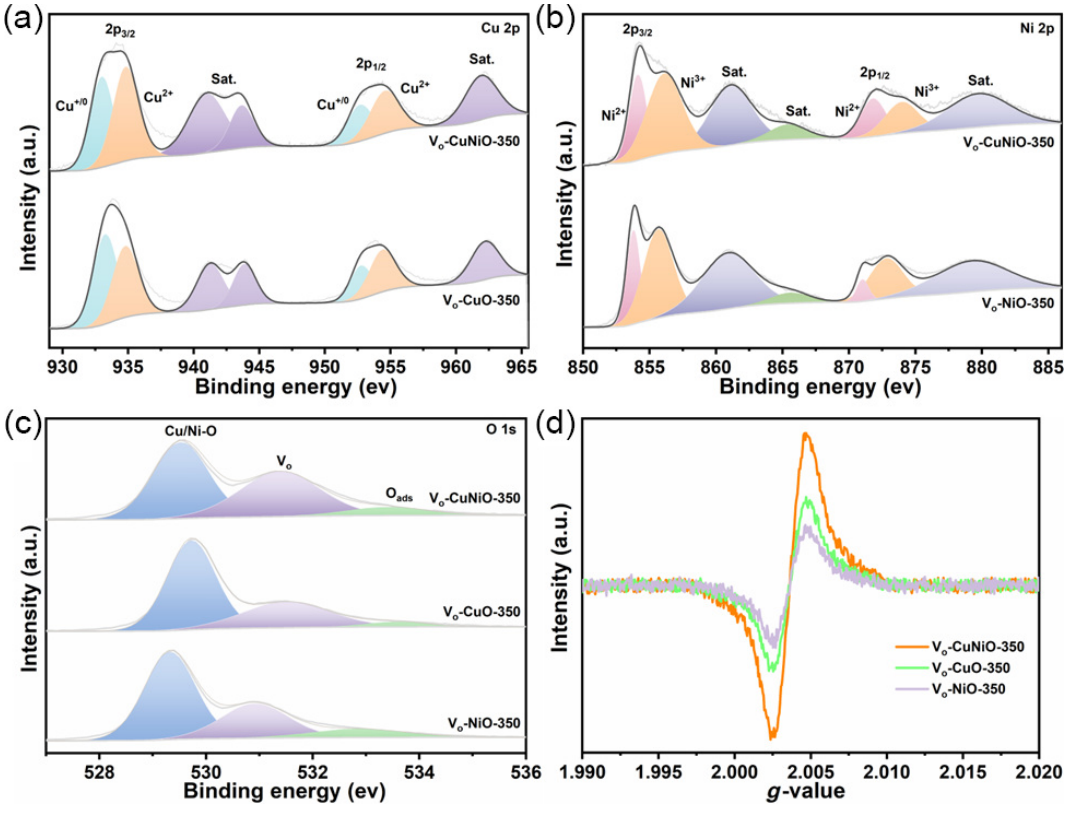


Figure 2 XPS and EPR characterizations. (a) Cu 2p XPS spectra of V_o-CuNiO-350 and V_o-CuO-350. (b) Ni 2p XPS spectra of V_o-CuNiO-350 and V_o-NiO-350. (c) O 1s XPS spectra of V_o-CuNiO-350, V_o-CuO-350, and V_o-NiO-350. (d) EPR spectra of Vo-CuNiO-350, V_o-CuO-350, and V_o-NiO-350.

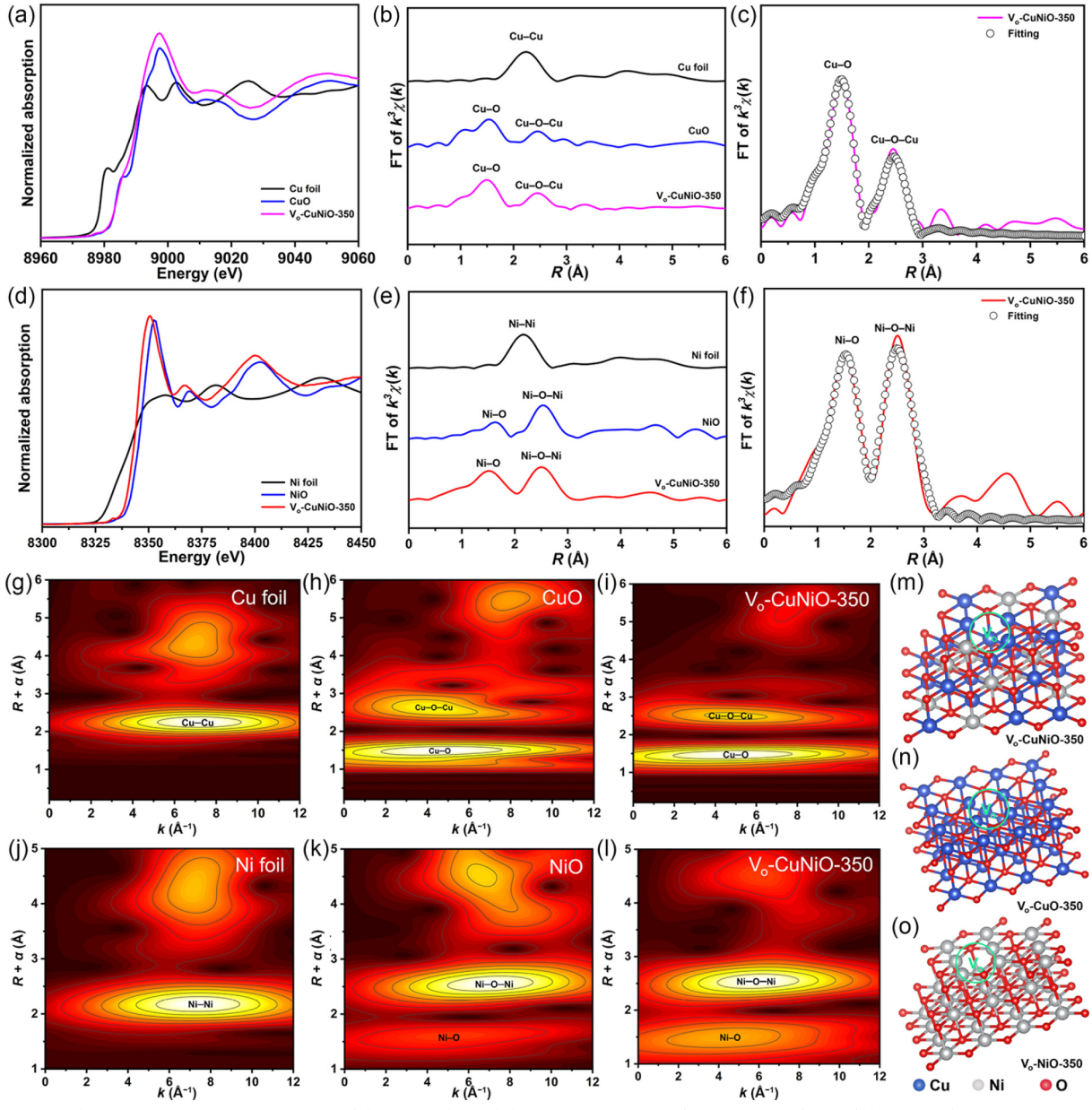


Figure 3 XAFS characterizations. (a) XANES spectra of the Cu K-edge and (b) FT-EXAFS spectra of Cu in *R*-space for Cu foil, CuO, and V_o-CuNiO-350. (c) Fitting results based on the Cu K-edge XANES spectra. (d) XANES spectra of the Ni K-edge and (e) FT-EXAFS spectra of Ni in *R*-space for Ni foil, NiO, and V_o-CuNiO-350. (f) Fitting results based on the Ni K-edge XANES spectra. ((g)–(i)) WT plots of the Cu atom environment for (g) Cu foil, (h) CuO, and (i) V_o-CuNiO-350. ((j)–(l)) WT plots of the Ni atom environment for (j) Ni foil, (k) NiO, and (l) V_o-CuNiO-350. ((m)–(o)) Possible structural models of different catalysts for (m) V_o-CuNiO-350, (n) V_o-CuO-350, and (o) V_o-NiO-350.

electrocatalytic NO_3RR activity. The NH_3 yield rates and FEs of the catalysts were then quantitatively evaluated by chronoamperometry (30 min of electrolysis) combined with UV–vis detection. After electrolysis at different potentials (–0.5––1.0 V vs. RHE), the electrolyte was diluted and analyzed by UV–vis to determine the concentrations of NH_3 and NO_2^- (Fig. S10 in the ESM). The electrocatalytic NO_3RR activities of V_o-CuNiO-*T* catalysts (*T* = 250, 300, 350, 400, and 500 °C) prepared at different calcination temperatures were systematically investigated (Fig. S11 in the ESM). The effect of calcination temperature on NO_3RR activity was initially assessed by LSV. Among the samples, V_o-CuNiO-350 exhibited the largest difference in current density with and without NO_3^- (Fig. S11(a) in the ESM). At –0.8 V vs. RHE, the FEs of V_o-CuNiO-250, V_o-CuNiO-300, V_o-CuNiO-350, V_o-CuNiO-400, and V_o-CuNiO-450 were 80.2%, 84.7%, 94.9%, 78.4%, and 75.7%, respectively (Fig. S11(b) in the ESM). The V_o-CuNiO-350 also showed the highest NH_3 yield rate (Fig. S11(c) in the ESM) and the lowest by-product NO_2^- concentration (Fig. S11(d) in the ESM), indicating that 350 °C is the optimal calcination temperature for achieving the best NO_3RR performance. The electrocatalytic results obtained at low applied potentials (–0.4–0 V vs. RHE) revealed both extremely low FEs and negligible NH_3 yield rates (Fig. S12 in the ESM), suggesting that the majority of electrons were diverted toward competing side reactions rather than participating in the NO_3RR. Moreover, these findings collectively indicate that, within the examined potential range, the thermodynamic driving force for

NO_3RR is insufficient. Furthermore, the electrocatalytic performances of the V_o-CuNiO-350 catalysts under varying NO_3^- concentrations and pH conditions were systematically investigated. Both the FEs and the NH_3 yield rates increased progressively with rising NO_3^- concentration, indicating that higher NO_3^- availability favors the electrocatalytic NO_3RR (Fig. S13 in the ESM). Subsequently, the catalytic activity of V_o-CuNiO-350 was evaluated across a range of pH values. The results revealed enhanced activity under acidic conditions; however, catalytic performance declined as the pH increased (Fig. S14 in the ESM). This trend suggests that insufficient proton supply under alkaline conditions impedes the hydrogenation steps critical to NH_3 formation, thereby suppressing overall activity. Notably, as a metal oxide catalyst, V_o-CuNiO-350 is susceptible to dissolution in strongly acidic media, which would inevitably compromise its structural stability and recyclability. Thereby, all electrocatalytic NH_3 synthesis experiments in this study were conducted in a neutral electrolyte for V_o-CuNiO-350, V_o-CuO-350, and V_o-NiO-350. As shown in Fig. 4(a), the current response of V_o-CuNiO-350 increased significantly upon the addition of NO_3^- compared with that without NO_3^-, confirming their high NO_3RR activity. For V_o-CuNiO-350, the FE for NH_3 followed a volcanic trend, reaching a maximum of 94.9% at −0.8 V vs. RHE, with an NH_3 yield rate of 377.1 μmol·h^{-1}·cm^{-2} and a partial current density of approximately 84.5 mA·cm^{-2}. Even at −1.0 V vs. RHE, the FE remained above 92%, while the NH_3 yield rate increased to 480.9 μmol·h^{-1}·cm^{-2} (Fig. 4(b) and Fig. S15 in the ESM), which can be attributed to the enhanced competition from the hydrogen evolution reaction at more negative potentials [58].

For V_o-CuO-350, both the NH_3 yield rate and FE gradually decreased as the potential increased (Fig. S16(a) in the ESM). In contrast, V_o-NiO-350 showed a very low NH_3 yield rate that slightly decreased with increasing potential, and its FE for NH_3 production remained around 55% (Fig. S16(b) in the ESM). Under optimal conditions (−0.8 V vs. RHE, 0.5 M Na_2SO_4 + 0.1 M $NaNO_3$), V_o-CuNiO-350 maintained stable NO_3RR activity over 10 consecutive electrolysis cycles, with only minor fluctuations in NH_3 yield rates and FEs (Fig. 4(c)). The V_o-CuNiO-350 catalysts after 10 cycles (Fig. S17 in the ESM) and 20 h of long-term stability test (Figs. S18 and S19 in the ESM) were characterized by XRD, TEM, and XPS. The crystallinity, morphology, and metal valence state of the samples did not change significantly after 10 cycles. The *i*–*t* curve for 20 h of long-term stability test by using V_o-CuNiO-350 as catalyst (at −0.8 V vs. RHE) indicated that the current density loss rate is approximately 5%, which shows that the V_o-CuNiO-350 catalyst is still very stable (Fig. S18 in the ESM). The XRD result (Fig. S19(a) in the ESM) indicated that the crystallinity of the catalyst decreases. The TEM images indicate that the catalyst still maintains an urchin-like hollow structure after 20 h, without obvious collapse (Fig. S19(b) in the ESM). Further XPS results (Figs. S19(c) and S19(d), and Table S6 in the ESM) show that with the extension of the

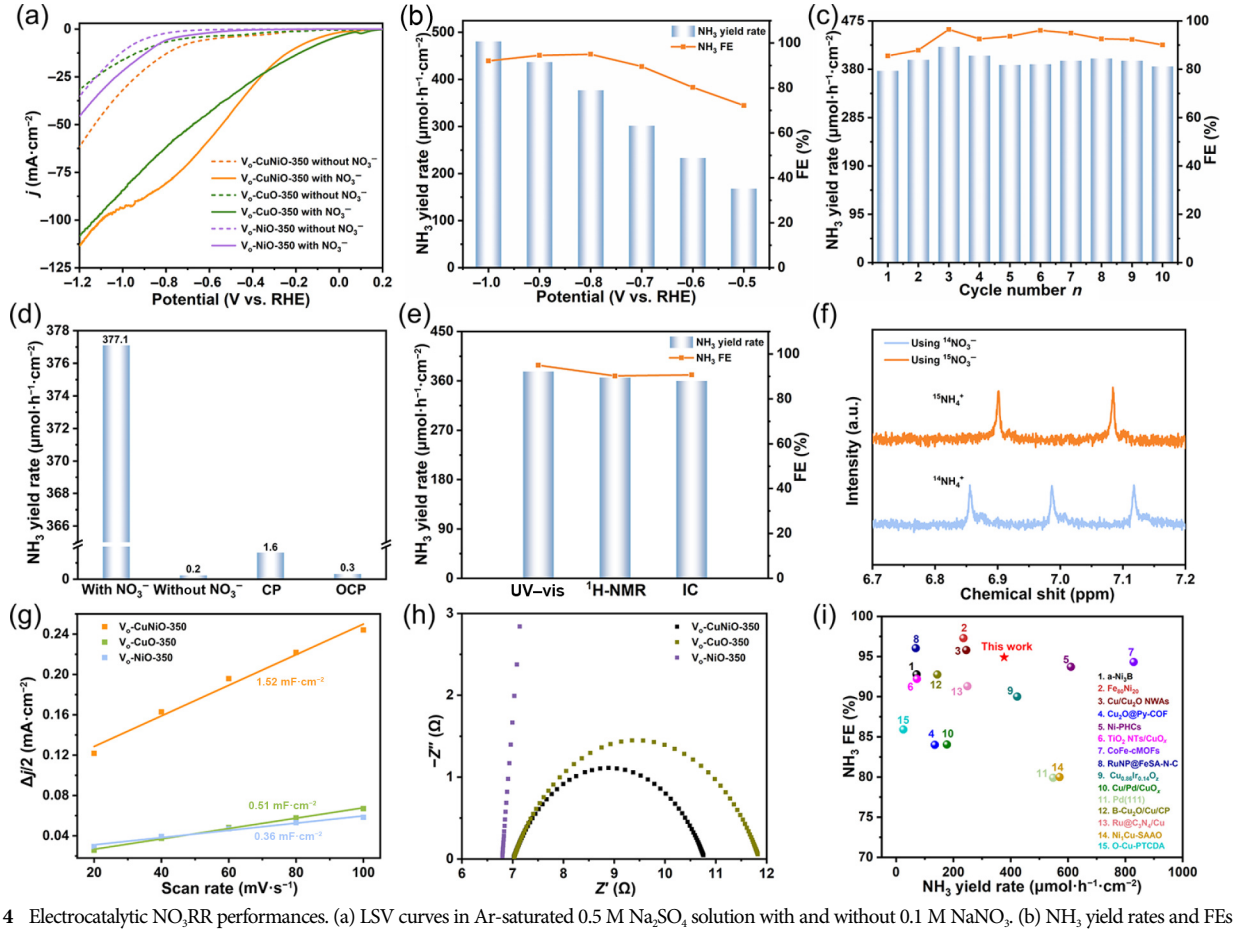


Figure 4 Electrocatalytic NO_3RR performances. (a) LSV curves in Ar-saturated 0.5 M Na_2SO_4 solution with and without 0.1 M $NaNO_3$. (b) NH_3 yield rates and FEs of V_o-CuNiO-350 using NO_3^- as the nitrogen source. (c) Cycling stability of V_o-CuNiO-350 at −0.8 V vs RHE. (d) Comparison of NH_3 yield rates under four different conditions. (e) Comparison of NH_3 yield rates and FEs measured by UV–vis, ^{1}H-NMR, and IC methods. (f) ^{1}H NMR spectra of products over V_o-CuNiO-350 with $^{14}NO_3^-$ or $^{15}NO_3^-$ as nitrogen source. (g) C_{dl} values and (h) Nyquist plots of V_o-CuNiO-350, V_o-CuO-350, and V_o-NiO-350. (i) Comparison of the NO_3RR performance of V_o-CuNiO-350 with previously reported catalysts.

stability test time, the Cu^{2+} species in the catalyst only decrease from 60.0% to 54.8%, and the Ni^{3+} species only decrease from 65.2% to 61.1%. These results prove that in V_o-CuNiO-350, Cu and Ni do not undergo extensive reduction at a negative potential, and the introduction of Ni keeps Cu in a high oxidation state. The above results fully prove that the structure of the V_o-CuNiO-350 catalyst has high stability and recyclability.

Control experiments were also performed using V_o-CuNiO-350 in Na_2SO_4 with and without $NaNO_3$, on blank carbon paper (CP), and under open-circuit potential (OCP). The NH_3 yield rates at −0.8 V vs. RHE after 30 min of electrolysis were 377.1, 0.2, 1.6, and 0.3 μmol·h^{-1}·cm^{-2} for the tested samples, respectively (Fig. 4(d)). The negligible NH_3 production in the control groups confirms that NO_3^- is the exclusive nitrogen source. To further verify the origin and quantify NH_3 production, ^{1}H nuclear magnetic resonance (NMR) spectroscopy (Figs. S20(a) and S20(b) in the ESM) and ion chromatography (IC, Figs. S20(c) and S20(d) in the ESM) methods were employed. The NH_3 amounts determined by ^{1}H NMR and IC closely matched with those obtained from the UV–vis method (Fig. 4(e)). Meanwhile, the by-product NO_2^- was also quantitatively analyzed by IC method (Fig. S21 in the ESM), and the results were basically consistent with those of the UV–vis method. The above results prove that the UV–vis method is reliable for the quantitative analysis of the produced NH_3 and NO_2^- [59, 60]. To confirm the nitrogen source and exclude contamination from the catalyst or environment, isotope-labeling experiments were performed using $Na^{15}NO_3$ and $Na^{14}NO_3$. The ^{1}H NMR spectra of the electrolyte with $Na^{15}NO_3$ showed characteristic doublets for $^{15}NH_4^+$, while that with $Na^{14}NO_3$ exhibited triplets for $^{14}NH_4^+$ (Fig. 4(f)), confirming that the nitrogen in NH_3 originates exclusively from nitrate rather than from external contamination [61]. To further confirm the relationship between the produced $^{15}NH_3$ and isotopes, the $^{15}NH_3$ FEs and yield rates at different $Na^{15}NO_3$ concentrations were systematically studied (Fig. S22 in the ESM). The results indicated that both the Faradaic efficiency and the $^{15}NH_3$ production rate increased with the increase of isotope concentration. On the one hand, this result further ruled out the possibility that the synthesized NH_3 was contaminated by other nitrogen sources. On the other hand, it also confirmed that all the synthesized NH_3 was originated from nitrate.

To identify the origin of the catalyst's activity, the electrochemical active surface area (ECSA) and charge-transfer kinetics were evaluated using double-layer capacitance (C_{dl}) and electrochemical impedance spectroscopy (EIS) measurements. The C_{dl}, derived from cyclic voltammetry at different scan rates (Fig. S23 in the ESM), was 1.52 mF·cm^{-2} for V_o-CuNiO-350, higher than that of V_o-CuO-350 (0.51 mF·cm^{-2}) and V_o-NiO-350 (0.36 mF·cm^{-2}) (Fig. 4(g)). Based on the C_{dl} values, the normalized ECSA values of different catalysts were obtained (Table S7 in the ESM). The ECSA values of V_o-CuNiO-350, V_o-CuO-350, and V_o-NiO-350 are 38, 12.75, and 9 cm^2, respectively. Therefore, it is evident that V_o-CuNiO-350 exhibits the highest specific activity, further confirming its superior catalytic performance. Similarly, EIS analysis showed a smaller charge-transfer resistance for V_o-CuNiO-350 compared with the single-metal oxides (Fig. 4(h)). These results indicate that the V_o-CuNiO-350 enhance the exposure of active sites, leading to an increased electrochemical active surface area and faster electrocatalytic kinetics for NO_3RR [62, 63]. Consistently, V_o-CuNiO-350 exhibited significantly higher NH_3 yield rate and FE than the monometallic oxides, thereby indicating a synergistic catalytic effect at the Cu–O–Ni interfacial sites [64, 65]. Moreover, compared with previously reported catalysts, V_o-CuNiO-350 shows excellent NO_3RR performance, with favorable FE and NH_3 yield rates (Fig. 4(i) and Table S8 in the ESM).

To gain deeper insight into the intrinsic electrocatalytic mechanism of NO_3RR, *in-situ* ATR-FTIR spectroscopy was employed to monitor reactive intermediates during electrocatalysis. Several characteristic peaks corresponding to key intermediates were observed in the potential range of −0.4–−1.1 V (Table S9 in the ESM) [59]. As shown in Fig. 5(a) and Fig. S24 in the ESM, the ATR-FTIR spectra of all three catalysts exhibited a peak for $*NH_2$, a crucial precursor for NH_3 formation, appearing at 1126 cm^{-1} for V_o-CuNiO-350, at 1167 cm^{-1} for V_o-CuO-350, and at 1097 cm^{-1} for V_o-NiO-350 [66]. A peak near 1220 cm^{-1} is attributed to the asymmetric stretching of N–O in $*NO_2$, observed at 1243 cm^{-1} for V_o-CuNiO-350, at 1246 cm^{-1} for V_o-CuO-350, and at 1246 cm^{-1} for V_o-NiO-350 [67]. Notably, V_o-CuNiO-350 showed the strongest $*NO_2$ absorption, whereas V_o-CuO-350 required a lower applied potential to activate NO_3^- reduction. An additional peak at 1560 cm^{-1} indicates the formation of *NO intermediates, confirming the consumption of NO_3^- (1336 cm^{-1}) along with the concurrent generation of NO_2^- and NO [68, 69]. Furthermore, a pronounced increase in absorption at 1632 cm^{-1} reflects the abundant availability of protons at catalytic sites for NH_3 formation, with V_o-NiO-350 showing higher intensity than V_o-CuO-350 [70]. For V_o-CuNiO-350, characteristic peaks corresponding to $*NH_2$ (1126 cm^{-1}) and $*NH_4^+$ (1446 cm^{-1}) were observed, thereby confirming NH_3 generation during electrocatalytic NO_3RR [71]. Figure 5(b) shows the time-dependent *in-situ* ATR-FTIR spectra of V_o-CuNiO-350 recorded during electrolysis at −0.8 V over 30 min (2-min intervals). The presence of key intermediates such as $*NO_2$, *NO, $*NH_2$, and $*NH_4^+$ was observed, indicating that copper active sites facilitate the conversion of NO_3^- to NO_2^-, while nickel active sites mainly accelerate the subsequent hydrogenation steps enabling efficient reduction of nitrate to ammonia [65, 72].

In-situ ATR-FTIR analysis shows that the NO_3RR proceeds through key intermediates of $*NO_3$, $*NO_2$, *NO, and $*NH_2$. EPR measurements confirm the presence of oxygen vacancies, and NO_3RR performance was found to increase with the number of vacancies, thereby indicating that oxygen vacancies play a vital role in enhancing catalytic activity. To further understand this enhancement, DFT calculations were conducted. A CuO model with an oxygen vacancy was constructed by removing a single O atom from the slab surface. Then, one-third of the Cu atoms were substituted with Ni to create an Ni-doped CuO model with an oxygen vacancy (denoted as V_o-CuNiO-350, Fig. S25(a) in the ESM). In the V_o-CuNiO-350 catalyst, there are three different oxygen-bridged interface sites, such as Cu–O–Cu, Ni–O–Ni, and Cu–O–Ni interfacial sites. Here, the newly formed bimetallic Cu–O–Ni interfacial sites are emphasized for their significant role in the electrocatalytic NO_3RR. To gain deeper insight into the role of Ni doping, a CuO slab with an oxygen vacancy but without Ni doping was constructed for comparison (denoted as V_o-CuO-350, Fig. S25(b) in the ESM). To illustrate the role of Cu, an NiO slab with oxygen vacancies was also modeled (denoted as V_o-NiO-350, Fig. S25(c) in the ESM). To examine the effect of oxygen vacancies, a CuNiO slab with Ni doping but without oxygen vacancies was constructed (Fig. S25(d) in the ESM). The V_o-CuNiO-350 and CuNiO slabs were built by replacing one-third of the Cu atoms in the corresponding V_o-CuO-350 and CuNiO models with Ni.

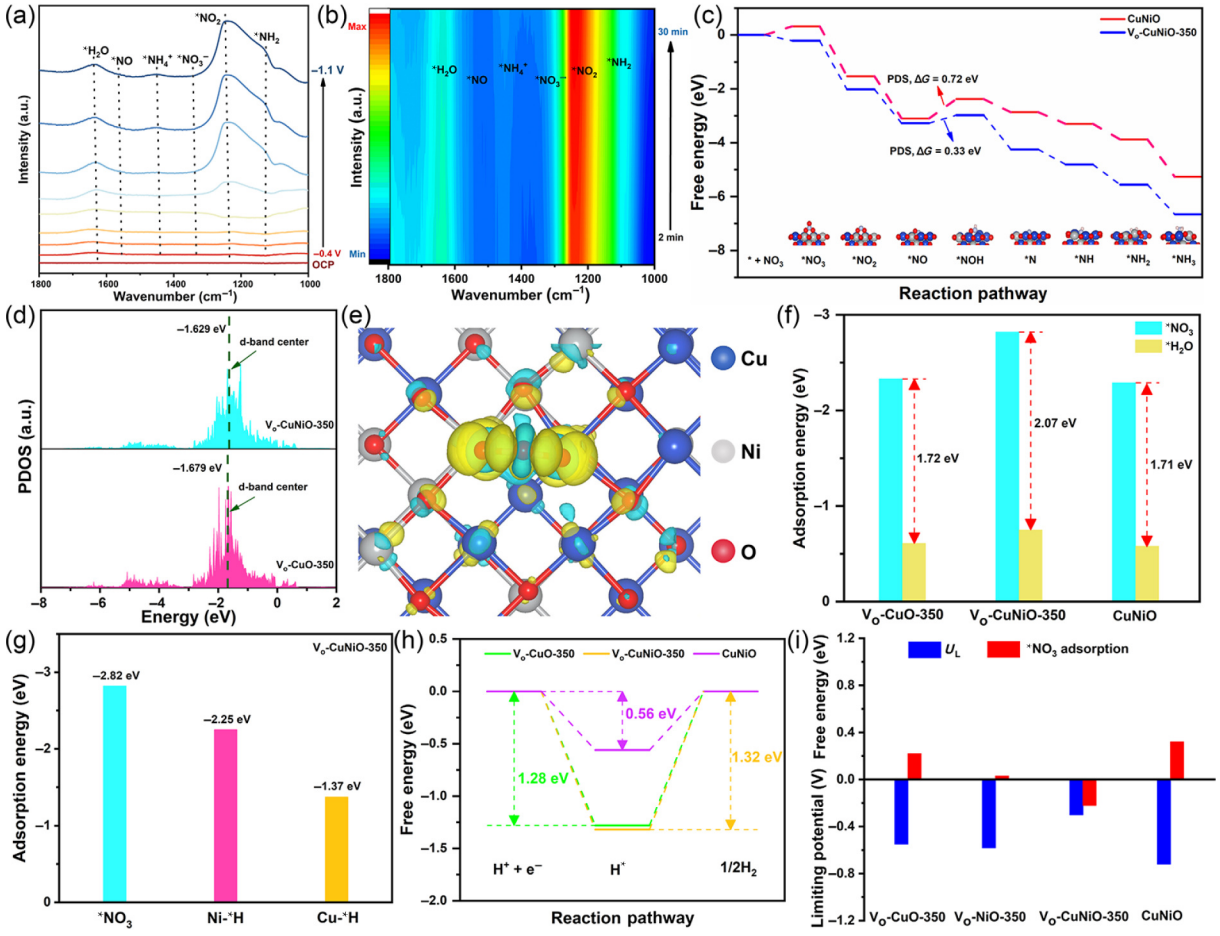


Figure 5 *In-situ* ATR-FTIR spectroscopy and DFT calculations revealing the origin of intrinsic activity. (a) *In-situ* ATR-FTIR spectra at different potentials and (b) at different time points (2-min intervals) during electrocatalytic NO_3RR. (c) Comparison of free energy diagram and reaction pathways for NO_3RR to NH_3 on V_o-CuNiO-350 and CuNiO. Insets show the PDSs and optimized structures of various intermediates (blue, gray, red, light gray, and white spheres represent Cu, Ni, O, N, and H atoms, respectively). (d) PDOS and the d-band center of the Cu 3d orbital for V_o-CuNiO-350 and V_o-CuO-350 models. (e) Charge density difference for NO_3^- adsorption on V_o-CuNiO-350 (blue and yellow represent regions of charge accumulation and depletion, respectively; isosurface value = 0.005 e·Å^{-3}). (f) Comparison of $*NO_3$ and $*H_2O$ adsorption energies on V_o-CuO-350, V_o-CuNiO-350, and CuNiO. (g) Adsorption energies of $*NO_3$ and *H on V_o-CuNiO-350. (h) Free energies of HER on V_o-CuO-350, V_o-CuNiO-350, and CuNiO. (i) Limiting potential for NO_3RR and adsorption free energy of $*NO_3^-$ on different catalyst models.

The NO_3^- reduction reaction pathway, Gibbs free-energy diagram for each step, and the geometric structures of intermediates are presented in Fig. 5(c) and Fig. S26 in the ESM. The reaction proceeds via the sequence: $*NO_3$ →$*NO_2$ → *NO → *NHO → *N → *NH → $*NH_2$→ $*NH_3$. The Gibbs free-energy diagram shows that the potential-determining step (PDS) has a limiting potential of 0.72 eV on CuNiO, which decreases to 0.33 eV on V_o-CuNiO-350, highlighting the positive effect of oxygen vacancies on NO_3RR performance. As shown in Fig. S27 in the ESM, the adsorption of $*NO_3$ was evaluated at different sites on the V_o-CuNiO-350 surface: site 1, at the center of the oxygen vacancy; site 2, at the edge of the oxygen vacancy; and site 3, far from the oxygen vacancy. The calculated adsorption energies were −2.33, −2.82, and −2.29 eV, respectively, indicating that the optimal site for initial $*NO_3^-$ adsorption is at the edge of the oxygen vacancy (site 2, Fig. S27 in the ESM). This provides clear evidence of the true active site for NO_3 reduction on V_o-CuNiO-350. As shown in Fig. S28 in the ESM, NO_3^- is adsorbed at the edge of the oxygen vacancy in a side-on configuration, with two of its O atoms simultaneously bonded, one to an Ni atom and the other to a Cu atom. Figure S29 in the ESM presents the crystal orbital Hamilton population (−COHP) analysis for $*NO_3$ adsorption on V_o-CuNiO-350. The integrated COHP (ICOHP) values for the Ni–O and Cu–O bonds are −1.80 and −1.70 eV, respectively, indicating a clear covalent characteristic. Ni doping strengthens the O–metal interaction, thereby enhancing $*NO_3$ adsorption on V_o-CuNiO-350. The electronic structures of V_o-CuO-350 and V_o-CuNiO-350 were further analyzed to assess the effect of Ni doping. The partial density of states (PDOS) profiles are shown in Fig. 5(d). Upon introducing Ni sites, the electronic density of the Cu d-band near the Fermi level shifts upward compared with V_o-CuO-350, thereby indicating greater electron transfer from antibonding to bonding orbitals in the V_o-CuNiO-350 model. A corresponding shift of the Cu 3d-band center is also observed, showing that Ni doping promotes the upward movement of the Cu d-band, which enhances bonding with adsorbed intermediates. This provides a clear explanation for the strengthened $*NO_3$ adsorption and the reduced energy barrier of the PDS upon Ni incorporation. Furthermore, the charge density difference analysis (Fig. 5(e)) reveals significant charge transfer between the Cu–O–Ni vacancy site and $*NO_3$. As shown in Fig. 5(f), in the initial stage of NO_3^- adsorption, V_o-CuNiO-350 exhibits decreased Gibbs free energies, indicating spontaneous nitrate adsorption at the active site. In contrast, CuNiO without oxygen vacancies and V_o-CuO-350

without Ni doping show a slight increase in Gibbs free energy during NO_3^- adsorption, suggesting poor activation of the nitrate reactant on these surfaces. These results demonstrate that oxygen vacancies and Ni doping synergistically promote stable adsorption and efficient activation of NO_3^- on V_o-CuNiO-350 (Fig. 5(i)). In the subsequent reaction steps, the potential-limiting step (PLS) for V_o-CuNiO-350 is the hydrogenation of *NO to *NHO, which aligns well with our experimental observations. Notably, compared with the free energy profile of V_o-CuO-350, the introduction of Ni atoms significantly lowers the energy barrier for the *NO → *NHO hydrogenation step, resulting in the superior NO_2RR performance of V_o-CuNiO-350. Comparison of the Gibbs free-energy diagrams for V_o-CuNiO-350 and CuNiO further highlights the effect of oxygen vacancies on NO_3RR performance (Fig. 5(c)). Without vacancies, NO_3^- reduction on CuNiO is much less efficient, even worse than that of V_o-CuO-350 without Ni doping, demonstrating that oxygen vacancies play a crucial role in enhancing NO_3RR activity.

The $*NO_3$ adsorption energies shown in Fig. 5(g) provide clear evidence for the superior NO_3^- adsorption capability of V_o-CuNiO-350, which can be attributed to two factors. First, the stronger Ni–O bond enhances the binding of reactants to the Ni atom, resulting in an asymmetric adsorption configuration of nitrate on V_o-CuNiO-350. Second, electron donation from Cu and Ni to the O atom of $*NO_3$ at the Cu–O–Ni vacancy site enables effective activation of $*NO_3$ compared with CuNiO (Fig. 5(e)). This not only promotes stable adsorption of subsequent intermediates but also reduces the reaction energy barrier of the PDS.

To further investigate the mechanism behind the high selectivity of V_o-CuNiO-350, the competitive adsorption energies of $*NO_3$ and $*H_2O$ on the catalyst surfaces of V_o-CuO-350, V_o-CuNiO-350, and CuNiO were compared (Fig. 5(f)). V_o-CuNiO-350 exhibits the most negative adsorption energy for $*NO_3$ and the largest difference between $*NO_3$ and $*H_2O$ adsorption energies (2.07 eV vs. 1.72 and 1.71 eV), indicating that Ni doping strengthens $*NO_3$ adsorption and promotes preferential occupation of active sites by $*NO_3$ over $*H_2O$. The adsorption energies of $*NO_3$ and *H on V_o-CuNiO-350 (Fig. 5(g)) show that $*NO_3$ binds more strongly than *H on both Cu and Ni sites. As shown in Fig. 5(h), the hydrogen evolution reaction (HER) is effectively suppressed on V_o-CuNiO-350 compared with V_o-CuO-350 (without Ni doping) and CuNiO (without oxygen vacancies). The preferential adsorption of $*NO_3$ on the active sites of V_o-CuNiO-350 explains its high selectivity for NH_3 production over the HER, which aligns well with the high FE observed experimentally. In contrast, as shown in Fig. S30 in the ESM, V_o-NiO-350 cannot effectively suppress HER. Furthermore, Fig. S31 in the ESM shows that NH_3 desorption from V_o-NiO-350 is difficult owing to its high desorption energy. These two factors together account for the poor NO_3RR performance of V_o-NiO-350 compared with the other catalysts.

In practical industrial wastewater treatment, the stripping method is widely used for NH_3 recovery, enabling its conversion into valuable products [73]. In this work, Ar gas was bubbled through the post-electrolysis solution at 60 °C to efficiently strip the electrochemically generated NH_3. The stripped NH_3 was then captured in 2 M HCl, and the resulting HCl solution containing NH_4^+ was processed via continuous rotary evaporation to produce ammonium chloride (NH_4Cl). Notably, 56.1 mg of NH_4Cl was collected after 4 h of electrolysis. XRD analysis (Fig. 6(a)) confirmed the high purity of the product, thereby indicating that approximately 70% of the electrolytically generated NH_3 was successfully converted into NH_4Cl without detectable impurities. These results demonstrate that this method is a promising approach for recovering nitrogen fertilizers from wastewater.

Furthermore, the Zn-NO_3^- battery is considered an environmentally friendly energy system, as it enables simultaneous electricity generation and conversion of waste nitrate (NO_3^-) into value-added NH_3 [74, 75]. In this work, a Zn-NO_3^- battery was constructed using catalyst-loaded carbon paper as the cathode and Zn foil as the anode (Fig. 6(b)). The open-circuit voltage (OCV) of the V_o-CuNiO-350/CP||Zn battery reached ~ 1.763 V vs. Zn/Zn^{2+}, compared with 1.750 and 1.634 V for the V_o-CuO-350/CP||Zn and V_o-NiO-350/CP||Zn batteries, respectively (Fig. 6(c)). After a 3600-s stability test, all three batteries showed only minor OCV fluctuations, demonstrating good operational durability. Discharge polarization curves revealed that the output current increased gradually as the voltage decreased. The V_o-CuNiO-350/CP||Zn battery achieved a maximum power density of 2.88 $mW{\cdot}cm^{-2}$, nearly three and four times higher than those of the V_o-CuO-350/CP||Zn and V_o-NiO-350/CP||Zn batteries (0.97 and 0.75 $mW{\cdot}cm^{-2}$), respectively, demonstrating its potential as an efficient power source for electronic devices (Fig. 6(d)). The discharge stability was further evaluated at various current densities. As shown in Fig. 6(e), the V_o-CuNiO-350/CP||Zn battery maintained excellent electrochemical stability across current densities of 0.1, 0.2, 0.4, 0.6, 0.8, 1, and 2 $mA{\cdot}cm^{-2}$, highlighting its superior rate capability. Long-term cycling stability was assessed via galvanostatic charge–discharge measurements, with the device operating continuously for over 25 h without significant widening of the charge/discharge voltage window, confirming the excellent durability of the V_o-CuNiO-350/CP||Zn battery (Fig. 6(f)). Taken together, these results highlight the superior performance of the V_o-CuNiO-350 catalyst and its great potential for application in Zn-NO_3^- batteries.

3 Conclusions

In summary, we developed a sea-urchin-like V_o-CuNiO-350 bimetallic catalyst via a scalable solvothermal-calcination method. Its hollow nanosphere morphology enhances electrolyte contact and mass transport, while Cu–O–Ni interfaces and abundant oxygen vacancies synergistically promote NO_3^- adsorption and activation. The V_o-CuNiO-350 catalyst achieves an NH_3 FE of 94.9% at −0.8 V and maintains more than 92% at −1.0 V, outperforming monometallic oxides (V_o-CuO-350 and V_o-NiO-350). Its stability over 10 cycles and high C_{dl} (1.52 $mF{\cdot}cm^{-2}$) confirm efficient utilization of active sites. *In-situ* ATR-FTIR spectroscopy and DFT calculations revealed that oxygen vacancies and oxygen-bridged multi-interface sites (especially the newly constructed Cu–O–Ni interface sites) in V_o-CuNiO-350 work synergistically to optimize intermediate adsorption and promote the reduction of NO_3^- to NH_3. The catalyst enables efficient NH_3 recovery as NH_4Cl and powers high-performance Zn-NO_3^- batteries (2.88 $mW{\cdot}cm^{-2}$), thereby demonstrating dual functionality in environmental remediation and energy conversion. This work highlights interfacial engineering and defect control as key strategies for advancing electrocatalytic nitrate-to-ammonia technologies.

Electronic Supplementary Material: Supplementary material (experimental sections, Figs. S1–S31, and Tables S1–S9) is available

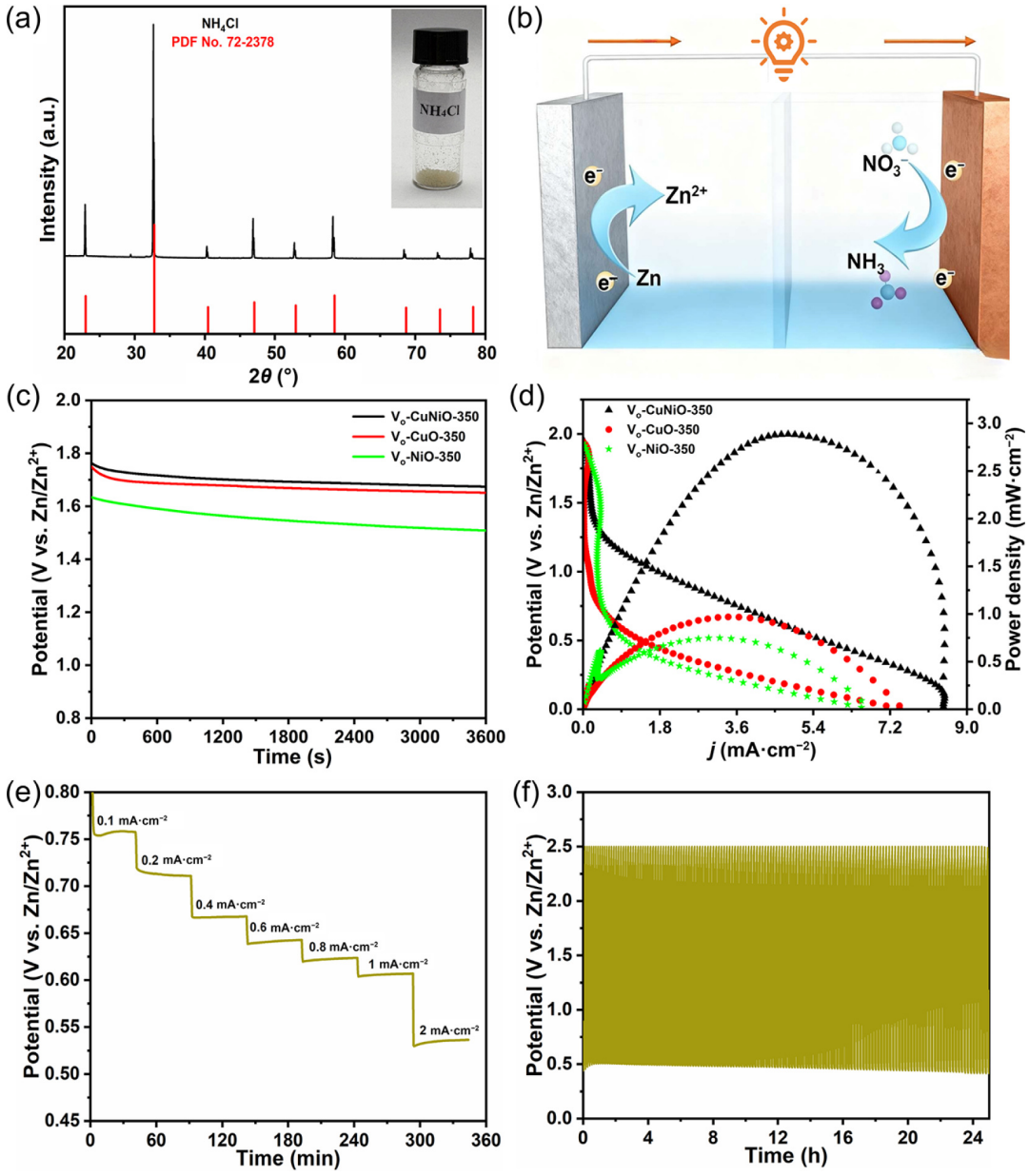


Figure 6 (a) Photograph and XRD pattern of NH_4Cl obtained via the stripping method. (b) Schematic illustration of the Zn-NO_3^- battery based on the NO_3RR. (c) Open-circuit voltage of the Zn-NO_3^- battery. (d) Discharge polarization and power density curves. (e) Discharge profiles at different current densities. (f) Long-term charge–discharge cycling performance.

in the online version of this article at https://doi.org/10.26599/NR.2026.94908769.

Data availability

All data needed to support the conclusions in the paper are presented in the manuscript and the Electronic Supplementary Material. Additional data related to this paper may be requested from the corresponding author upon request.

Acknowledgements

This work was financially supported by the National Natural Science Foundation of China (No. 22375005), the Outstanding Young Teacher Cultivation in Anhui Province Department of Education (No. YQZD2023031) , the Natural Science Research Project of Anhui Province Education Department (No. 2023AH051116), the Open Project of Key Laboratory of Metallurgical Emission Reduction & Resources Recycling of Ministry of Education (No. JKF21-03), the Open Fund of Anhui Provincial Key Laboratory of Advanced Catalysis and Energy Materials (No. ZD2025A06), the open project of State Key Laboratory of Materials-Oriented Chemical Engineering (No. SKL-MCE-24B012), and the Open Fund of State Key Laboratory of Heavy Oil Processing (No. SKLHOP202202009). We thank the Shanghai Synchrotron Radiation Facility of BL11B (https://cstr.cn/31124.02.SSRF.BL11(B)) for the assistance on XAFS measurements. We thank LetPub (www.letpub.com.cn) for its linguistic assistance during the preparation of this manuscript.

Declaration of competing interest

All the contributing authors report no conflict of interests in this work.

Author contribution statement

L. Q.: Data curation, project administration, validation, writing and revising manuscript, experimental design. Z. X. T.: Data curation, validation. G. Q. C.: Data curation. Q. Q. Z.: Data curation. C. X. L.: Data curation. Y. X. W.: Funding acquisition. M. F. Y.: Funding acquisition. B. B. J.: Funding acquisition. Y. W. T.: Funding acquisition, revising manuscript. G. Z. H.: Supervision, project administration, revising manuscript. G. H. F.: Software, writing manuscript. K. L. W.: Supervision, project administration, funding acquisition, revising manuscript, experimental design. All the authors have approved the final manuscript.

Use of AI statement

None.

References

[1] Xiong, Y. C.; Wang, Y. H.; Zhou, J. W.; Liu, F.; Hao, F. K.; Fan, Z. X. Electrochemical nitrate reduction: Ammonia synthesis and the beyond. *Adv. Mater.* **2024**, *36*, 2304021.

[2] Theerthagiri, J.; Park, J.; Das, H. T.; Rahamathulla, N.; Cardoso, E. S. F.; Murthy, A. P.; Maia, G.; Vo, D. V. N.; Choi, M. Y. Electrocatalytic conversion of nitrate waste into ammonia: A review. *Environ. Chem. Lett.* **2022**, *20*, 2929–2949.

[3] Wang, Y. T.; Zhou, W.; Jia, R. R.; Yu, Y. F.; Zhang, B. Unveiling the activity origin of a copper-based electrocatalyst for selective nitrate reduction to ammonia. *Angew. Chem., Int. Ed.* **2020**, *59*, 5350–5354.

[4] Li, Y.; Wei, J. S.; Lin, H. X.; Guo, Y.; Lu, X. H.; Liu, S. Q.; Liu, H. Z.; Tang, M. Y.; Zhou, J.; Li, Y. Y. Hollow square Ni-doped copper oxide catalyst boosting electrocatalytic nitrate reduction. *ACS Catal.* **2025**, *15*, 1672–1683.

[5] MacFarlane, D. R.; Cherepanov, P. V.; Choi, J.; Suryanto, B. H. R.; Hodgetts, R. Y.; Bakker, J. M.; Ferrero Vallana, F. M.; Simonov, A. N. A roadmap to the ammonia economy. *Joule* **2020**, *4*, 1186–1205.

[6] Liu, Y. T.; Liu, K.; Wang, P. F.; Jin, Z. Y.; Li, P. P. Electrocatalytic upcycling of nitrogenous wastes into green ammonia: Advances and perspectives on materials innovation. *Carbon Neutral.* **2023**, *2*, 14.

[7] Zhong, W.; Hong, Q. L.; Ai, X.; Zhang, C.; Li, F. M.; Li, X. F.; Chen, Y. RhNi bimetallenes with lattice-compressed Rh skin towards ultrastable acidic nitrate electroreduction. *Adv. Mater.* **2024**, *36*, 2314351.

[8] Soloveichik, G. Electrochemical synthesis of ammonia as a potential alternative to the Haber-Bosch process. *Nat. Catal.* **2019**, *2*, 377–380.

[9] Chen, F. Y.; Wu, Z. Y.; Gupta, S.; Rivera, D. J.; Lambeets, S. V.; Pecaut, S.; Kim, J. Y. T.; Zhu, P.; Finfrock, Y. Z.; Meira, D. M. et al. Efficient conversion of low-concentration nitrate sources into ammonia on a Ru-dispersed Cu nanowire electrocatalyst. *Nat. Nanotechnol.* **2022**, *17*, 759–767.

[10] Jin, D. L.; Chen, A. Q.; Lin, B. L. What metals should be used to mediate electrosynthesis of ammonia from nitrogen and hydrogen from a thermodynamic standpoint. *J. Am. Chem. Soc.* **2024**, *146*, 12320–12323.

[11] Cao, Y.; Yuan, S. B.; Meng, L. H.; Wang, Y. Y.; Hai, Y.; Su, S. D.; Ding, W. M.; Liu, Z. Y.; Li, X. M.; Luo, M. Recent advances in electrocatalytic nitrate reduction to ammonia: Mechanism insight and catalyst design. *ACS Sustainable Chem. Eng.* **2023**, *11*, 7965–7985.

[12] Chen, G. F.; Yuan, Y. F.; Jiang, H. F.; Ren, S. Y.; Ding, L. X.; Ma, L.; Wu, T. P.; Lu, J.; Wang, H. H. Electrochemical reduction of nitrate to ammonia via direct eight-electron transfer using a copper-molecular solid catalyst. *Nat. Energy* **2020**, *5*, 605–613.

[13] Yin, H. B.; Dong, F.; Su, H. W.; Zhuang, Z. C.; Wang, Y. L.; Wang, D. S.; Peng, Y.; Li, J. H. Unraveling the activity trends and design principles of single-atom catalysts for nitrate electrocatalytic reduction. *ACS Nano* **2023**, *17*, 25614–25624.

[14] Xia, J. K.; Xu, J. W.; Yu, B.; Liang, X.; Qiu, Z.; Li, H.; Feng, H. J.; Li, Y. F.; Cai, Y. J.; Wei, H. Y. et al. A metal-sulfur-carbon catalyst mimicking the two-component architecture of nitrogenase. *Angew. Chem., Int. Ed.* **2024**, *63*, e202412740.

[15] Hao, J. C.; Wang, T. D.; Yu, R. H.; Cai, J.; Gao, G. H.; Zhuang, Z. C.; Kang, Q.; Lu, S. L.; Liu, Z. H.; Wu, J. S. et al. Integrating few-atom layer metal on high-entropy alloys to catalyze nitrate reduction in tandem. *Nat. Commun.* **2024**, *15*, 9020.

[16] Yu, K. D.; Zhou, K. J.; Liang, S.; Xu, Y. Q.; Luo, T. R.; Leng, Y. M.; Chen, Z. B. Single atom–support interactions for highly efficient electrochemical nitrate reduction to ammonia: Fundamentals and recent progress. *Nano Res.* **2026**, *19*, 94908183.

[17] Wang, Y. H.; Xu, A. N.; Wang, Z. Y.; Huang, L. S.; Li, J.; Li, F. W.; Wicks, J.; Luo, M. C.; Nam, D. H.; Tan, C. S. et al. Enhanced nitrate-to-ammonia activity on copper-nickel alloys via tuning of intermediate adsorption. *J. Am. Chem. Soc.* **2020**, *142*, 5702–5708.

[18] Wang, Y. Y.; Bao, T.; Chen, L. Y.; Zhang, C. Q.; Wang, J.; Zou, Y. Y.; Xi, Y. M.; Li, Z. J.; Yu, C. Z.; Liu, C. Boosting nitrate-to-ammonia conversion over copper-based electrocatalysts by facilitating hydrogenation and product desorption. *Angew. Chem., Int. Ed.* **2025**, *64*, e202509090.

[19] Zhang, Z. B.; Yu, K. L.; Wang, H.; Bian, Z. Y. Advances in electrocatalytic nitrate reduction to ammonia over Cu-based catalysts. *Environ. Res.* **2025**, *274*, 121123.

[20] Zhang, K. E.; Liu, Y.; Pan, Z. F.; Xia, Q.; Huo, X. Y.; Esan, O. C.; Zhang, X.; An, L. Cu-based catalysts for electrocatalytic nitrate reduction to ammonia: Fundamentals and recent advances. *EES Catal.* **2024**, *2*, 727–752.

[21] Liu, Z. R.; Wang, J. J.; Li, Y. F.; Qiu, C. L.; Liang, Y. H.; Wang, J. C. Synergistic copper single-atoms and nanoparticles *in-situ* generated towards nitrate electroreduction to ammonia. *Nano Res.* **2026**, *19*, 94908370.

[22] Guo, Y. J.; Liu, Z. Y.; Zhou, D. Y.; Zhang, M. Y.; Zhang, Y.; Li, R. Z.; Liu, S. L.; Wang, D. S.; Dai, Z. H. Competition and synergistic effects of Ru-based single-atom and cluster catalysts in electrocatalytic reactions. *Sci. China Mater.* **2024**, *67*, 1706–1720.

[23] Guo, X. T.; Yu, J. D.; Ren, S. J.; Gao, R. T.; Wu, L. M.; Wang, L. Controlled defective engineering on CuIr catalyst promotes nitrate selective reduction to ammonia. *ACS Nano* **2024**, *18*, 24252–24261.

[24] Deng, Y. L.; Mo, X. Y.; Lai, S. K. M.; Haw, S. C.; Au-Yeung, H. Y.; Tse, E. C. M. Mechanical and covalent tailoring of copper catenanes for selective aqueous nitrate-to-ammonia electrocatalysis. *J. Am. Chem. Soc.* **2025**, *147*, 14316–14325.

[25] Wu, L. M.; Zhang, L. B.; Feng, J. Q.; Jia, S. H.; Wang, R. H.; Song, X. N.; Ma, X. D.; Zhu, Q. G.; Kang, X. C.; Qian, Q. L. et al. Intermittent electrolysis enabling enhanced efficiency and stability for nitrate reduction. *Chem* **2025**, *11*, 102591.

[26] Liu, Y. L.; Zhuang, Z. C.; Liu, Y. X.; Liu, N. Y.; Li, Y. X.; Cheng, Y. Y.; Yu, J. W.; Yu, R. H.; Wang, D. S.; Li, H. T. Shear-strained Pd single-atom electrocatalysts for nitrate reduction to ammonia. *Angew. Chem., Int. Ed.* **2024**, *63*, e202411396.

[27] Liu, Y. X.; Zhang, X.; Feizpoor, S.; Chen, H. C.; Li, L. F.; Zuo, Y. P.; Tian, S. J.; Liu, M. N.; Hu, W. Y.; Humayun, M. et al. Embedded Fe–Cu pairs enable tandem nitrate-to-ammonia electroreduction. *Adv. Mater.* **2026**, *38*, e14840.

[28] Zhou, C.; Huang, Y. T.; Liu, C. Q.; Wang, C. X.; Fang, W. J.; Xia, H.; Song, Y. B.; Ji, M. W.; Lu, F. S. B-doped carbon nanotubes for enhanced adsorption of NO_3^- and promoted electrocatalysis on

transformation nitrate into ammonia. *Nano Res.*, in press, DOI: 10.26599/nr.2026.94908512.

[29] Fu, X. X.; Guo, H.; Si, D. H.; Zhu, H. J.; Lan, Y. Y.; Huang, Y. B.; Cao, R. Hydrogen-bond mediated electrocatalytic nitrate reduction to ammonia over metal-organic frameworks with industrial current density. *Chem. Sci.* **2025**, *16*, 13503–13513.

[30] Liu, X. F.; Xu, C.; Chen, X.; Liu, J.; Jiang, F. X.; Cheng, X. F.; Xu, Q. F.; Lu, J. M. Modulation of Cu electronic structure to accelerate the conversion of key intermediates for electrocatalytic ammonia synthesis. *ACS Catal.* **2025**, *15*, 6141–6149.

[31] Liu, P.; Yan, J. Y.; Huang, H.; Song, W. B. Cu/Co bimetallic conductive MOFs: Electronic modulation for enhanced nitrate reduction to ammonia. *Chem. Eng. J.* **2023**, *466*, 143134.

[32] Wang, X. H.; Hong, Q. L.; Shao, L. Y.; Zhai, Q. G.; Jiang, Y. C.; Ai, X.; Chen, Y.; Li, S. N. Copper-nickel oxide nanosheets with atomic thickness for high-efficiency sulfur ion electrooxidation assisted nitrate electroreduction to ammonia. *Adv. Funct. Mater.* **2024**, *34*, 2408834.

[33] Zhang, J. Y.; Liu, L.; Hu, N.; Wang, R. X.; An, Y. L. Accelerating proton coupled electron transfer by confined Cu–Ni bimetallic clusters for boosting electrochemical hydrodeoxygenation of nitrate. *Appl. Catal. B: Environ.* **2025**, *371*, 125195.

[34] Wang, J. C.; Ma, J. Q.; Du, H. X.; Ma, R. G.; Wang, J. C. Electrifying nitrate conversion: Dual-metal-site catalysts as a game-changer for sustainable NH_3 production. *Nano Res.* **2026**, *19*, 94907798.

[35] Wei, J. L.; Wang, J. L.; Yu, W. Q.; Li, J. W.; Yang, Y.; Wang, Y. P.; Li, N.; Xu, R. D.; Yang, L. J.; Li, G. X. et al. Dual active site accelerated hydrogenation facilitates efficient electrochemical reduction of nitrate to ammonia. *Appl. Catal. B: Environ. Energy* **2025**, *378*, 125629.

[36] Zhou, Y. X.; Xia, R. L.; Hao, R.; Li, S. J.; Chen, X. Y.; Liu, Y. P.; Li, W. Complementary enhancement between noble metal-like Fe_3C and Cu^0/Cu^+ sites to fulfil highly selective wide-potential nitrate electroreduction to ammonia. *J. Energy Chem.* **2025**, *108*, 713–723.

[37] Jang, W.; Oh, D.; Lee, J.; Kim, J.; Matthews, J. E.; Kim, H.; Lee, S. W.; Lee, S.; Xu, Y.; Yu, J. M. et al. Homogeneously mixed Cu–Co bimetallic catalyst derived from hydroxy double salt for industrial-level high-rate nitrate-to-ammonia electrosynthesis. *J. Am. Chem. Soc.* **2024**, *146*, 27417–27428.

[38] Wang, C. H.; Liu, Z. Y.; Peng, Q. X.; Xing, D. D.; Hu, T.; Du, F.; Li, C. M.; Ma, R. G.; Yang, H. B.; Guo, C. X. Bimetallic $Cu_{11}Ag_3$ nanotips for ultrahigh yield rate of nitrate-to-ammonium. *Angew. Chem., Int. Ed.* **2025**, *64*, e202415259.

[39] Wang, Y. H.; Hao, F. K.; Xu, H. M.; Sun, M. Z.; Wang, X. X.; Xiong, Y. C.; Zhou, J. W.; Liu, F.; Hu, Y. B.; Ma, Y. B. et al. Interfacial water structure modulation on unconventional phase non-precious metal alloy nanostructures for efficient nitrate electroreduction to ammonia in neutral media. *Angew. Chem., Int. Ed.* **2025**, *64*, e202508617.

[40] Li, Z. Y.; Shi, Z. C.; Ou, Y. G.; Zhong, L. X.; Yan, C. S.; Zhang, C.; Song, K.; Liu, H. J.; Liu, D. B.; Song, P. et al. Pulsed electrocatalysis driven efficient ammonia synthesis by facilitating *NOOH formation and balancing *H supply. *Angew. Chem., Int. Ed.* **2025**, *64*, e202510287.

[41] Jia, G. H.; Sun, Y. Q.; Liu, P. L.; Luo, J. Q.; Zhang, P.; Wei, Y. C.; Song, W. Y.; Li, Z. X.; Zhao, Z.; Liu, J. N-doped bamboo-like carbon nanotube-encapsulated CuNi alloy to enrich nitrate and boost electrochemical ammonia synthesis. *Nano Res.* **2025**, *18*, 94907265.

[42] Guo, J. Y.; Zhang, L. H.; Guo, Y. B.; Shi, C. X.; Han, A. L.; Wang, D. S.; Yu, F. S. Oxygen-incorporation-engineered interfacial water modulation on single-atom Cu sites for enhanced dilute nitrate electroreduction. *Angew. Chem., Int. Ed.* **2026**, *65*, e16401.

[43] Zhu, C. X.; Yang, J. R.; Zhang, J. W.; Wang, X. Q.; Gao, Y.; Wang, D. S.; Pan, H. G. Single-atom materials: The application in energy conversion. *Interdiscip. Mater.* **2024**, *3*, 74–86.

[44] Wu, K. L.; Zhu, D. D.; Dai, X. L.; Wang, W. N.; Zhong, X. Y.; Fang, Z. B.; Peng, C.; Wei, X. W.; Qian, H. S.; Chen, X. L. et al. Bimetallic oxide $Cu_{1.5}Mn_{1.5}O_4$ cage-like frame nanospheres with triple enzyme-like activities for bacterial-infected wound therapy. *Nano Today* **2022**, *43*, 101380.

[45] Yuan, P. W.; Guo, S. H.; Gao, S. Q.; Wang, J.; Chen, W. Q.; Li, M.; Ma, K. Y.; Wang, N.; Liu, F.; Cheng, J. P. Influence of Ni/Cu ratio in nickel copper carbonate hydroxide on the phase and electrochemical properties. *J. Alloys Compd.* **2019**, *780*, 147–155.

[46] Li, J. N.; Zhao, T. T.; Shirolkar, M. M.; Li, M.; Wang, H. Q.; Li, H. N. CuO/ZnO heterojunction nanorod arrays prepared by photochemical method with improved UV detecting performance. *Nanomaterials* **2019**, *9*, 790.

[47] Lv, T. Z.; Yang, L. K.; Hong, C.; Zhu, Y. H.; Shen, J. H.; Li, C. Z. Electronic interaction at Cu–O–Ni heterointerface promotes electrocatalytic nitrate reduction to ammonia and zinc-nitrate battery. *Adv. Sci.* **2026**, *13*, e21252.

[48] Tian, H.; Wang, X. H.; Luo, W. S.; Ma, R. D.; Yu, X.; Li, S. J.; Kong, F. T.; Cui, X. Z.; Shi, J. L. Construction of an electron-transfer channel via Cu–O–Ni to inhibit the overoxidation of Ni for durable methanol oxidation at industrial current density. *Chem. Sci.* **2024**, *15*, 11013–11020.

[49] Chen, S. H.; Ye, C. L.; Wang, Z. W.; Li, P.; Jiang, W. J.; Zhuang, Z. C.; Zhu, J. X.; Zheng, X. B.; Zaman, S.; Ou, H. H. et al. Selective CO_2 reduction to ethylene mediated by adaptive small-molecule engineering of copper-based electrocatalysts. *Angew. Chem., Int. Ed.* **2023**, *62*, e202315621.

[50] Ma, F. Y.; Zhang, P. F.; Zheng, X. B.; Chen, L.; Li, Y. R.; Zhuang, Z. C.; Fan, Y. M.; Jiang, P.; Zhao, H.; Zhang, J. W. et al. Steering the site distance of atomic Cu−Cu pairs by first-shell halogen coordination boosts CO_2-to-C_2 selectivity. *Angew. Chem., Int. Ed.* **2024**, *63*, e202412785.

[51] Liu, Q.; Xie, L. S.; Liang, J.; Ren, Y. C.; Wang, Y. Y.; Zhang, L. C.; Yue, L. C.; Li, T. S.; Luo, Y. S.; Li, N. et al. Ambient ammonia synthesis via electrochemical reduction of nitrate enabled by $NiCo_2O_4$ nanowire array. *Small* **2022**, *18*, 2106961.

[52] Guan, S. Y.; Liu, Y. Y.; Liu, S. L.; Zhuang, Z. C.; Shen, R. F.; Zhang, H. H.; Liang, E. J.; Fan, Y. P.; Jiang, J. C.; Liu, B. Z. et al. MXene-supported Ru–Ni: A common active site for hydrolysis, hydrogen oxidation, and hydrogenation. *Angew. Chem., Int. Ed.* **2025**, *64*, e202506869.

[53] You, Y.; Chen, H. L.; Guo, J. Y.; Feng, Z. H.; Zhan, J. Y.; Yu, F. S.; Zhang, L. H. Structure reconstruction driven by oxygen vacancies forming P–$CoMoO_4$/$Co(OH)_2$ heterostructure boosting electrocatalytic nitrate reduction to ammonia. *Appl. Catal. B: Environ. Energy* **2025**, *363*, 124837.

[54] Tyagi, N. K.; Mahapatra, B. K.; Ghimire, S.; Manna, N.; Kumar, D.; Kumar, V.; Mukhopadhyay, K.; Singh, S. K. Theory-directed designing of an intrinsic-activity-modulated metal-doped copper oxide electrode for nitrate to ammonia synthesis. *ACS Appl. Energy Mater.* **2023**, *6*, 6111–6119.

[55] Chen, W. Z.; Su, H.; Chen, X. P.; Zheng, X.; Zou, Z. H.; Tang, J.; Zhang, M. S.; Wang, Q. X.; Ling, Y.; Li, J. F. Dual-polymer engineered Ni–O–Si interface catalysts for selective and durable electrocatalytic urea synthesis. *Nano Res.* **2026**, *19*, 94908251.

[56] Sun, C. Z.; Xiao, B. H.; Zhao, Q.; Zong, X. M.; Zeng, Y. X.; Cao, S. S.; Liu, Z. Q. *In situ* reconstructed Cu/$Cu_{2+1}O$/ZnO inverse opals accelerate electrocatalytic nitrate reduction kinetics for high power Zn-NO_3^- battery. *Adv. Mater.* **2025**, *37*, 2510680.

[57] Liu, X.; Cheng, X. T.; Zhao, H. L.; Liu, P. F.; Wang, Y. Q. $CuCo_2O_4$/CuO heterostructure with oxygen vacancies induced by plasma for electrocatalytic nitrate reduction to ammonia. *Inorg. Chem.* **2024**, *63*, 14093–14102.

[58] Zhang, K. E.; Sun, P. T.; Huang, Y. L.; Tang, M. C.; Zou, X. H.; Pan, Z. F.; Huo, X. Y.; Wu, J.; Lin, C. C.; Sun, Z. T. et al. Electrochemical nitrate reduction to ammonia on CuCo nanowires at practical level. *Adv. Funct. Mater.* **2024**, *34*, 2405179.

[59] Peng, C.; Wang, M. Y.; Li, S.; Zeng, X. Z.; Wang, J. Y.; Wang, W. H.; Zhang, Z. R.; Ye, M. F.; Wei, X. W.; Wu, K. L. et al. A general strategy based on hetero-charge coupling effect for constructing single-atom sites. *Angew. Chem., Int. Ed.* **2024**, *63*, e202408771.

[60] Yang, X. R.; Ma, L.; Wang, S. Q.; Hu, X. Y.; Li, B.; Li, W.; Wang, D. S.; Dai, Z. H. Electrochemiluminescence-based multiplex immunoassays for multianalyte bioanalysis: Signal encoding strategies and analytical perspectives. *Electrochem. Commun.* **2026**, *186*, 108130.

[61] You, X. C.; Xu, J. W.; Zhuang, Z. C.; Xia, J. K.; Wang, S. W.; Wei, H. Y.; Li, Y. F.; Cai, Y. J.; Xiang, H.; Yu, B. Ru-Ni alloy nanosheets as tandem catalysts for electrochemical reduction of nitrate to ammonia. *Nano Res.* **2024**, *17*, 4815–4824.

[62] Zhang, R.; Zhang, Y. Q.; Xiao, B.; Zhang, S. C.; Wang, Y. B.; Cui, H. L.; Li, C.; Hou, Y.; Guo, Y.; Yang, T. et al. Phase engineering of high-entropy alloy for enhanced electrocatalytic nitrate reduction to ammonia. *Angew. Chem., Int. Ed.* **2024**, *63*, e202407589.

[63] Mo, Z. H.; Ma, Z. H.; Ran, Y. J.; Wang, Y. G.; Li, T. H.; Sun, W.; Hu, W. H. NiO-incorporated Cu/Cu_2O nanowires for highly efficient electrochemical nitrate reduction to ammonia. *ChemSusChem* **2025**, *18*, e202401607.

[64] Bai, Z. H.; Li, X.; Ding, L.; Qu, Y. S.; Chang, X. H. Artificial Cu-Ni catalyst towards highly efficient nitrate-to-ammonia conversion. *Sci. China Mater.* **2023**, *66*, 2329–2338.

[65] Feng, Y.; Lv, X. W.; Wang, H. Y.; Wang, H.; Yan, F. X.; Wang, L.; Wang, H. Y.; Ren, J. T.; Yuan, Z. Y. *H species regulation of heterostructured Cu_2O/NiO nanoflowers boosting tandem nitrite reduction for high-efficiency ammonia production. *Adv. Funct. Mater.* **2025**, *35*, 2425687.

[66] Sun, H.; Xia, Z. X.; Qi, Y. Y.; Xu, Q.; Han, J. W.; Wu, J. H.; Qin, J. S.; Rao, H. Tandem Cu–Co sites in MOF-818 for efficient ammonia electrosynthesis from nitrate in neutral media. *ACS Catal.* **2025**, *15*, 16581–16590.

[67] Zhang, Z. D.; Wang, M.; Xing, H. R.; Zhou, X. C.; Gao, L.; Chen, S. Z.; Chen, Y. J.; Xu, H.; Li, W.; Yuan, S. et al. Efficient ammonia electrosynthesis from pure nitrate reduction via tuning bimetallic sites in redox-active covalent organic frameworks. *Angew. Chem., Int. Ed.* **2025**, *64*, e202505580.

[68] Zhou, B.; Tong, Y. W.; Yao, Y. C.; Zhang, W. X.; Zhan, G. M.; Zheng, Q.; Hou, W.; Gu, X. K.; Zhang, L. Z. Reversed I_1Cu_4 single-atom sites for superior neutral ammonia electrosynthesis with nitrate. *Proc. Natl. Acad. Sci. USA* **2024**, *121*, e2405236121.

[69] Wu, G. Z.; Zhang, W. Y.; Yu, R.; Yang, Y. D.; Jiang, J. D.; Sun, M. M.; Du, A. J.; He, W. H.; Dai, L.; Mao, X. et al. p-d orbital hybridization in Ag-based electrocatalysts for enhanced nitrate-to-ammonia conversion. *Angew. Chem., Int. Ed.* **2024**, *63*, e202410251.

[70] Dong, J. H.; Song, X. Z.; Chen, Y. X.; Gai, Z. X.; Yuan, Z.; Liu, D. K.; Tan, Z. Q.; Liu, A. M.; Wang, X. F.; Song, S. Y. Engineering Ce promoter to regulate H* species to boost tandem electrocatalytic nitrate reduction for ammonia synthesis. *Adv. Funct. Mater.* **2025**, *35*, 2422025.

[71] Wang, J. J.; Ou, Z. D.; Dong, C. B.; Su, M. Y.; Ali, A.; Kuklin, A. V.; Ågren, H.; Baryshnikov, G. V.; Liu, Y.; Zhao, X. et al. Electronic structure modulated by B-doped Cu promotes electrocatalytic nitrate reduction for ammonia production. *ACS Catal.* **2025**, *15*, 156–166.

[72] Wang, Y. L.; Yin, H. B.; Dong, F.; Zhao, X. G.; Qu, Y. K.; Wang, L. X.; Peng, Y.; Wang, D. S.; Fang, W.; Li, J. H. N-coordinated Cu-Ni dual-single-atom catalyst for highly selective electrocatalytic reduction of nitrate to ammonia. *Small* **2023**, *19*, 2207695.

[73] Cheng, Q. Y.; Liu, S. S.; He, Y. Z.; Wang, M. F.; Ji, H. Q.; Huan, Y. F.; Qian, T.; Yan, C. L.; Lu, J. M. Multivariate covalent organic frameworks with tailored electrostatic potential promote nitrate electroreduction to ammonia in acid. *Nat. Commun.* **2025**, *16*, 3717.

[74] Yang, X. H.; Zhou, Z. N.; Zou, Y. Y.; Kuang, J. Q.; Ye, D. W.; Zhang, S. S.; Gao, Q. Z.; Yang, S. Y.; Cai, X.; Fang, Y. P. Interface reinforced 2D/2D heterostructure of Cu-Co oxides/FeCo hydroxides as monolithic multifunctional catalysts for rechargeable/flexible zinc-air batteries and self-powered water splitting. *App. Catal. B: Environ.* **2023**, *325*, 122332.

[75] Yu, W. Q.; Yu, J. Y.; Huang, M.; Wang, Y. J.; Wang, Y. J.; Li, J. W.; Liu, H.; Zhou, W. J. Laser-controlled tandem catalytic sites of CuNi alloys with ampere-level electrocatalytic nitrate-to-ammonia reduction activities for Zn-nitrate batteries. *Energy Environ. Sci.* **2023**, *16*, 2991–3001.

This is an open access article under the terms of the Creative Commons Attribution 4.0 International License (CC BY 4.0, https://creativecommons.org/licenses/by/4.0/).

© The Author(s) 2026. Published by Tsinghua University Press.